Performance of rammed earth subjected to in-plane cyclic displacement

Romanazzi A.[1], Oliveira D.V.[2], Silva R.A.[3], Barontini A.[4], Mendes N.[5]

1. ISISE, Department of Civil Engineering, University of Minho, Guimarães, Portugal, aromanazzi89@gmail.com, https://orcid.org/0000-0003-1684-8826

2. ISISE, Department of Civil Engineering, University of Minho, Guimarães, Portugal, danvco@civil.uminho.pt, https://orcid.org/0000-0002-8547-3805

3. ISISE, Department of Civil Engineering, University of Minho, Guimarães, Portugal, ruisilva@civil.uminho.pt, https://orcid.org/0000-0002-1115-107X

4. ISISE, Department of Civil Engineering, University of Minho, Guimarães, Portugal, albe.barontini@gmail.com, https://orcid.org/0000-0001-8377-8149

5. ISISE, Department of Civil Engineering, University of Minho, Guimarães, Portugal, nunomendes@civil.uminho.pt, https://orcid.org/0000-0002-1796-686X

Abstract

Rammed earth structures are worldwide spread, both as architectural heritage and new constructions. Yet, rammed earth buildings present, in general, high seismic vulnerability. Despite the several studies conducted on the mechanical characterisation of rammed earth and on the numerical modelling of structural elements built with this material, further in-plane cyclic tests on rammed earth sub-assemblies are required to characterise their hysteretic behaviour. In this framework, an experimental program was conducted where cyclic in-plane tests were performed on a large-scale rammed earth wall. The geometry of the wall was defined to represent a sub-assembly commonly found in rammed earth dwellings from Alentejo (Southern Portugal). The wall was subjected to cyclic shear displacements with increasing amplitude, imposed in both positive and negative directions. To detect the dynamic properties of the wall and to assess the development of the structural damage, dynamic identification tests were conducted along the experimental programme. The results are analysed in terms of crack pattern, dynamic properties, displacement capacity, base shear performance and stiffness degradation. Further discussion is led on the dissipated energy, while a bi-linear and linear equivalent systems are proposed as simplified modelling approach. In conclusion, degradation of structural capacity was observed due to cyclic loads, while adequate energy dissipation and base shear coefficient were obtained.

Keywords: rammed earth, in-plane cyclic loading, energy-based analysis, dynamic identification, stiffness degradation, seismic capacity

1 Introduction

Earthen materials have been extensively used throughout several human civilizations, becoming part of their architectural heritage [1][2]. The popularity of earthen materials can be attributed to the local availability of the raw material, sustainability of the process, ease of building, adequate thermal and acoustic isolation, and low cost [3][4]. As consequence, various building techniques based on the use of soil have been developed, yet adobe, compressed earth blocks and rammed earth are among the most used nowadays. On the other hand, earthen buildings are characterised by high seismic vulnerability, which results from the low strength of the earthen material, high mass and lack of engineering approaches in design and building practices [5][6][7]. Thus, earthen structures are unable to sustain large inertial forces associated to moderate and strong ground motions, as demonstrated by recent earthquakes, such as the M_w 8.0 Pisco earthquake (Peru 2007), the M_w 6.3 Bam earthquake (Iran 2003), and the M_w 8.8 Maule earthquake (Chile 2010) [8][9].

Despite the nowadays widespread use of rammed earth as a building solution, the response of such structures is still not well known, particularly with regard to the in-plane behaviour of the walls under cyclic loads. In fact, several studies addressed the characterisation of mechanical properties of the rammed earth as a building material, such as Young's modulus, shear modulus, compressive and shear strength, among others [8][10][11][12][13][14][15]. Such properties are fundamental for the numerical modelling of rammed earth structures using simplified methods and assumptions, such as the linear elastic analysis while considering a homogeneous and isotropic material. Further investigations were focused on advanced numerical modelling of the seismic response of rammed earth structures [16][17][18][19][20][21][22][23], however such numerical studies were rarely validated with real observations. Despite the various experimental investigations on the mechanical behaviour of rammed earth as building material, the behaviour of a rammed earth walls may involve phenomena that cannot be rendered through simplified testing protocols. In that case, the experimental characterisation of the hysteretic behaviour of the structure requires more complex testing protocols, such as cyclic loading on large-scale structural components, which allow to assess the stiffness and strength degradation or energy dissipation [24]. The significance of such parameters lies on the fact that hysteretic properties permit to define simplified models for designing, while including the actual structural dissipative capacity, which otherwise would be only possible with sophisticated numerical models. Moreover, accurate seismic vulnerability assessments are fundamental to implement appropriate

strengthening solutions in rammed earth built heritage. As can be found in literature, only few experimental studies have been conducted on large-scale rammed earth walls due to the higher complexity and cost of such tests, while very few analyses have been focused on the dissipative capacity and stiffness degradation. In [25][26], a full-scale wall was tested under cyclic in-plane loads. The results showed that the earthen walls are brittle and their lateral load capacity decreases for low drift demands, while the shear capacity is controlled by the wall axial load and aspect ratio. In addition, rammed earth exhibits high energy dissipation capacity, while the lateral stiffness decreases rapidly at early stages of lateral displacements. Further experimental studies of the in-plane response of earthen walls were conducted in [23][27][28][29][30], however reduced-scale models of single walls were tested. In [31][32], the natural frequencies and mode shapes of rammed earth walls were detected by means of dynamic identification tests. Although such properties are valuable for numerical calibration of models in the determination of the boundary conditions and the elastic properties of the materials, they do not provide direct measurement on the hysteretic and dissipative capacity of the structure.

Considering such framework, an experimental program was conducted to investigate the in-plane cyclic performance of a rammed earth structural sub-assembly in the form of an I-shaped wall. The aim was to characterise the response and to evaluate the hysteretic properties of the wall under shear loads. These outcomes can be later assumed to further develop recommendations for practitioners while providing data for calibration of numerical models. At first the test setup is presented, describing the materials used to build the wall for the rammed earth in-plane test (hereinafter referred to as RE-IP) and the testing protocol. Subsequently, the experimental results are reported and discussed in terms of cracking pattern, dynamic characterisation, displacement capacity, base shear forces and strength decay. Further discussions address the stiffness degradation and energy dissipation, which allowed determining the equivalent damping coefficient. Therefore, equivalent elastic and elastic-perfectly plastic systems are proposed based on the experimental curves, according to simplified models for masonry structures [33][34][35][36].

2 Experimental program

2.1 Material and geometry of the sub-assembly

In order to analyse the in-plane behaviour of rammed earth walls of traditional single-storey buildings with timber roof, commonly found in Alentejo region (Southern Portugal), a reduced scale 1:1.25 sub-assembly was built with an I-shape geometry in plan. The geometric scale factor of $\lambda = 0.80$ was a limitation imposed by the laboratorial facilities (Fig. 1a). Thus,

the design of the in-plane cyclic tests considered the compliance with Cauchy's or Cauchy-Froude's similitude laws on the scaled geometry, stress-strain relationships of materials, mass and gravity forces, and boundary conditions [37]. Theoretically, a similitude scale law between the model and the real prototype structure allows to assume the structural response of a scaled model, including the damage patterns and failure mechanisms, to be similar to the behaviour observed in a real structure. Alentejo region was selected as main case study of the traditional rammed earth construction from Portugal, since a significant percentage of the Portuguese rammed earth dwellings are concentrated in this region [31]. The geometry of the sub-assembly was defined with basis on a preliminary survey investigation in the scope of the research project SafEarth [21]. Wing-walls were considered in the geometry, since no isolated walls are observed in the traditional buildings and because wings provide the necessary stability to the web-wall during in-plane cyclic loadings. Hence, the model consisted of two wing-walls with 120 cm length and a web-wall with 280 cm length, while the thickness of each was 40 cm and the height was 180 cm (Fig. 1a). The foundation of the model consisted of limestones embedded in a concrete layer of 10 cm thick cast on a steel plate. The plate included welded steel vertical connectors to impede sliding of the concrete layer and was properly fixed to the lab strong-floor with tie rods (Fig. 1b). The rammed earth wall was built by mechanical compaction of a moistened mixture of soil in layers of about 10 cm thick using a complete formwork made of timber panels (Fig. 1c). To this purpose, the raw soil was collected from Alentejo for sake of representativeness and characterised by means of geotechnical analysis, such as particle size distribution (PSD), Atterberg's limits and Standard Proctor test. The results showed elevated content of clay fraction and low dry density for a high optimal water content (OWC), which could cause crack due to shrinkage. Therefore, the raw soil was mixed with coarse sand and gravel in proportion of 40% of soil, 30% of sand and 30% of gravel, obtaining a composition made of 6% of clay, 9 % of silt, 38% of sand and 47% of gravel, and dry density of 2.02 g/cm^3 for a OWC of 12%. Such composition met the recommendations found in literature, e.g. [38]. Afterwards, compressive tests were performed on representative cylindrical specimens to assess the compressive strength (f_c) and the Young's modulus (E_{re}), which resulted in average values of 0.56 MPa (CoV = 13%) and 213 MPa (CoV = 33%), respectively. The experimental compressive strength was found similar to the design value suggested by the NZS 4297 [39]. The structural sub-assembly was demoulded immediately after achieving the full height of the walls, while the drying occurred for a period of about four months in laboratory conditions.

The test setup was designed to impose cyclic horizontal displacements at the top. Thus, two U-steel profiles were placed at each one of the wing-walls and were connected by two tie rods crossing them through holes created during the construction (Fig. 1a and Fig. 1d). The stiffness and contact surface of the steel profiles were designed to provide even distribution of the loads during the test and to avoid punching failure.

Accordingly, to simulate the scaled vertical load of a traditional timber roof, the wall was loaded with bags for a total weight of 11.77 kN after a drying period of four months. The in-plane cyclic displacements were applied by an actuator with 300 kN capacity, which was connected with a cylindrical hinge to the mock-up and with a spherical hinge to the reaction wall. An additional system was set to support the actuator in order to prevent the influence of its weight (Fig. 1e).
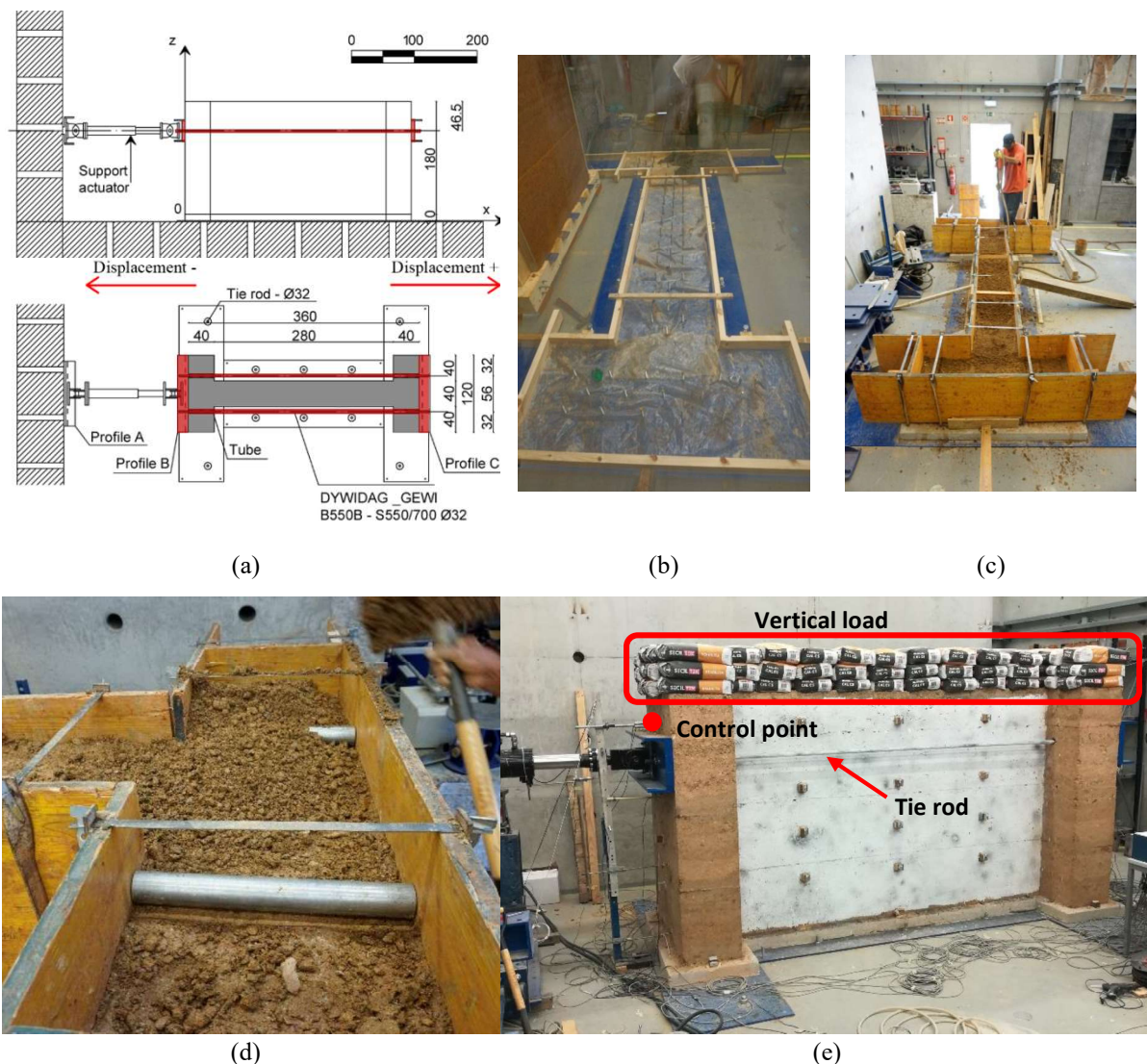

(a) (b) (c)

(d) (e)

Fig. 1 *Details of the rammed earth sub-assembly: a) geometry [cm], b) foundation, c) construction, d) negative for the holes used to introduce the tie rods, and e) general view*

2.2 Testing protocol

The loading-unloading cycles were conducted by controlling the displacement in the loading direction of a point at the top of the left wing (control point). The entire cyclic testing protocol considered increasing target displacements in both directions (positive and negative), and two repetitions for each positive-negative cycle, as indicated in Tab. 1. In addition, dynamic identification tests through Operational Modal Analysis (OMA) were performed to detect modal frequencies (f) and mode shapes (Φ) of the model and to track their evolution under increasing levels of damage, by means of sixteen accelerometers (model PCB 393B12, 0.15 to 1000 Hz frequency range, 10000 mV/g sensitivity, 8μg resolution). Each test consisted of two setups with two fixed reference sensors and fourteen moving sensors to acquire the response over a grid with 4x5 points (Fig. 2a). The disposition and orientation of the accelerometers were defined in order to identify the in-plane and out-of-plane behaviour of the wall. Additionally, four accelerometers were placed at the steel plate (G#), aiming at evaluating possible alterations in the boundary conditions of the wall along the tests (Fig. 2).

In OMA, the vibration of a structure is recorded under ambient excitation to identify its dynamic properties [40][41]. To guarantee the basic assumption of white noise and obtain accurate data resolution, the duration of each dynamic identification record was of 20 minutes and a sampling frequency 200 Hz was adopted. The ARTeMIS Modal software [42] was used to analyse the obtained signals. The dynamic properties depend on the structural stiffness, which in turn is affected by degradation of the materials or structural elements, such as alterations of geometry, aging, cracking or change in boundary conditions [43][44][45][47]. Therefore, the variation in the dynamic properties along the test was employed as an indicator of damage evolution. Dynamic identification tests were labelled as DI-RE-IP-#*number of test*.

The first dynamic identification test (DI-RE-IP-01) was performed on the model prior to any testing. Further, two dynamic identification tests were conducted, namely after the fifth cycle and at the end of the cyclic test protocol, which were named as DI-RE-IP-02 and DI-RE-IP-03, respectively (Tab. 1). It is specified that the testing protocol was carried out in consecutive phases; meaning that the loading was interrupted and the actuator disconnected once that each cycle was completed. In this way, the effect of the actuator on the dynamic identification tests was null.

Cycle	Rate [μm/s]	Δd [mm]	Drift [%]
DI-RE-IP-01			
1	2	± 0.2	0.01
2	5	± 0.4	0.02
3	5	± 0.8	0.04
4	15	± 1.2	0.07
5	30	± 2.4	0.13
DI-RE-IP-02			
6	60	± 3.6	0.19
7	60	± 4.8	0.27
DI-RE-IP-03			

As for monitoring deformations during the cyclic loading, a set of 4 LVDTs were placed at each wing-wall, measuring displacements in the loading direction along a vertical profile (LVDT-a1 to LVDT-d1, and LVDT-a5 to LVDT-d5); 4 additional LVDTs were placed horizontally at each inner corner to measure relative displacements between the wing-walls and the web-wall (LVDT-a2 to LVDT-d2, and LVDT-a4 to LVDT-d4). Further 3 LVDTs were set along the base of the wall to monitor the possible sliding at the foundation interface (LVDT-g1, LVDT-g2 and LVDT-g3). The deformations at the middle-third zone of the web-wall were also monitored using 6 LVDTs placed in horizontal, vertical, and diagonal alignments. The position of the LVDTs is illustrated in Fig. 2b.
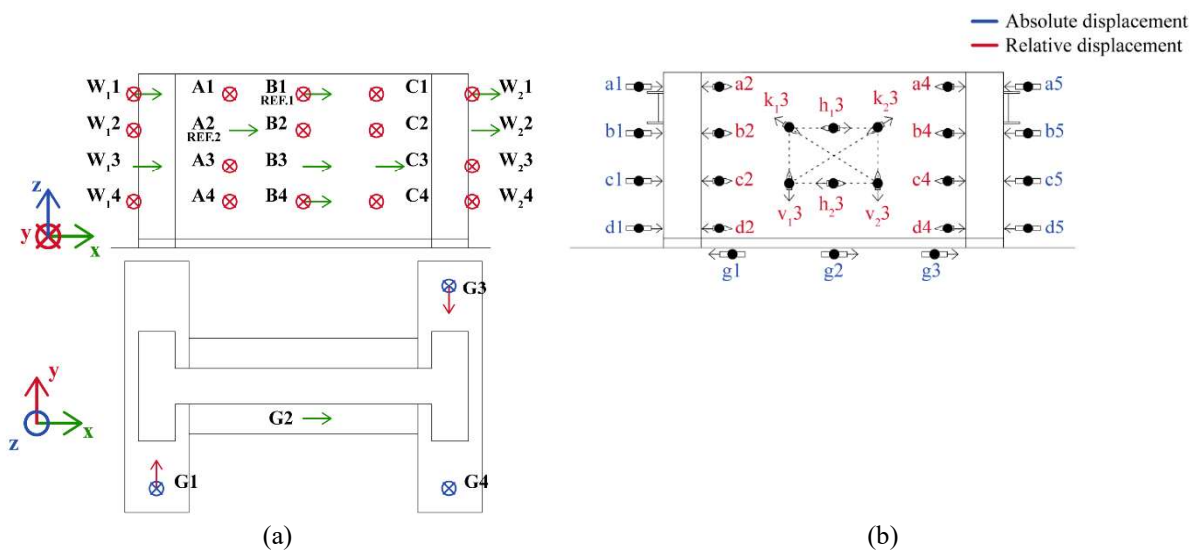

(a) (b)

Fig. 2 *Position of the sensors used to monitor accelerations and deformations: a) accelerometers (REF: references), and b) LVDTs*

3 Results and discussion

The results of the tests conducted on the rammed earth model RE-IP are presented and discussed in the subsequent sections, in terms of cracking pattern, dynamic properties, displacements, base shear coefficient, stiffness decay, energy-based analysis and proposal of bi-linear and linear equivalent systems.

3.1 Cracking pattern

The cracking pattern of the rammed earth model was monitored during the cyclic tests. Minor cracks were first observed on wing-walls close to the loading surface during the fifth cycle, however a main horizontal crack formed in the web-wall along one of the interfaces between layers at an early stage of the sixth cycle. Afterwards, further two diagonal cracks opened at the lower inner corner of the web-wall, connecting with the previous horizontal crack, as showed in Fig. 3.

It should be noted that three main types of failure modes are encountered when a general structural masonry wall is subjected to in-plane seismic loads, which depend on the geometry of the structural element and quality of materials, boundary restraints and acting loads [36]. In the case of low vertical loads, in-plane actions usually cause shearing and then sliding of two superimposed blocks, as the observed cracking pattern of the rammed earth wall. Therefore, the RE-IP wall subjected to in-plane loads responded as a non-homogeneous material as consequence of the low tensile and shear strength of the interface between layers, and low vertical loads.

Fig. 3 Cracking pattern of the RE-IP model

3.2 Dynamic properties

In the following analysis, the Enhanced Frequency Domain Decomposition (*EFDD*) method was adopted on the original undecimated signal. Three vibration modes were estimated

for the model before being tested (DI-RE-IP-01). The frequency of the first mode (f_1) is equal to 18.12 Hz and corresponds to the out-of-plane bending of the wall with single curvature (Fig. 4a); the frequency of the second mode (f_2) is equal to 24.46 Hz and it corresponds to the second out-of-plane bending mode of the wall with single curvature and the top corners out-of-phase (Fig. 4b); finally, the third mode presents a frequency (f_3) of 32.04 Hz and corresponds to the third out-of-plane bending mode with second curvature, in which the top corners and middle section of the wall are out-of-phase. (Fig. 4c).
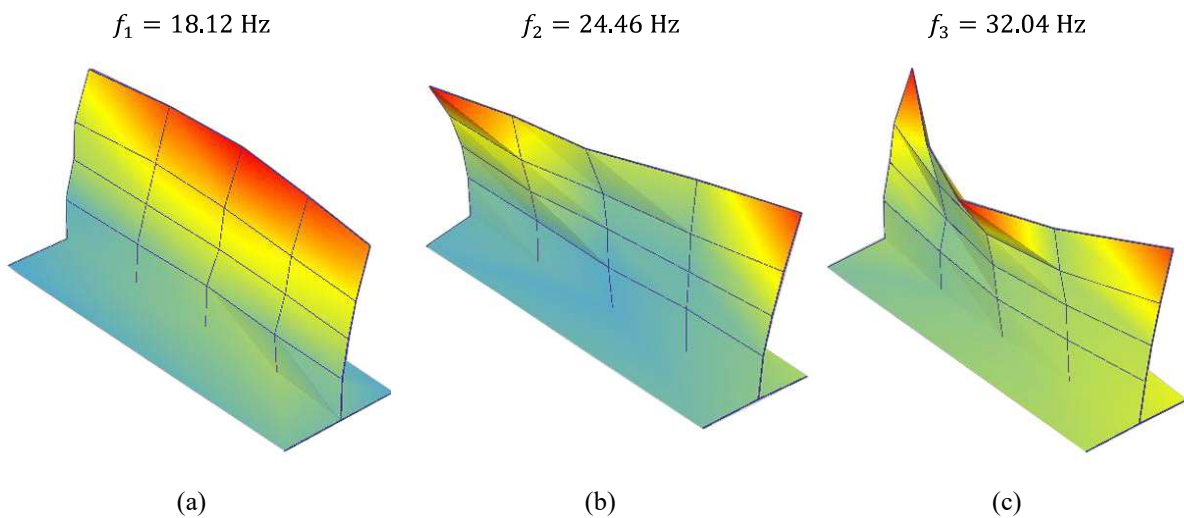
$f_1 = 18.12$ Hz $\qquad\qquad$ $f_2 = 24.46$ Hz $\qquad\qquad$ $f_3 = 32.04$ Hz

(a) $\qquad\qquad\qquad\qquad$ (b) $\qquad\qquad\qquad\qquad$ (c)

Fig. 4 *Natural vibration modes of the rammed earth model obtained from the DI-RE-IP-01 test: a) mode 1, b) mode 2, and c) mode 3*

The results of the dynamic identification DI-RE-IP-02 were similar to the results of DI-RE-IP-01 (no damage with possible minor influence of temperature variation). The natural frequencies of DI-RE-IP-02 are $f_1 = 18.24$ Hz, $f_2 = 24.66$ Hz and $f_3 = 32.75$ Hz, while the mode shapes associated to each natural frequency were analogous to the correspondent mode shapes of the first dynamic identification test. The last dynamic identification (DI-RE-IP-03) was performed after the main crack occurrence, resulting in a decrease of the first natural frequency to $f_1 = 17.08$ Hz (Fig. 5a) and the appearance of new mode shapes for the second and third natural frequencies. The mode shapes related to $f_2 = 29.92$ Hz and $f_3 = 32.80$ Hz of the DI-RE-IP-03 correspond to in-plane bending of the top of the web-wall (Fig. 5b and Fig. 5c), which suggests the cracks originated new local modes.
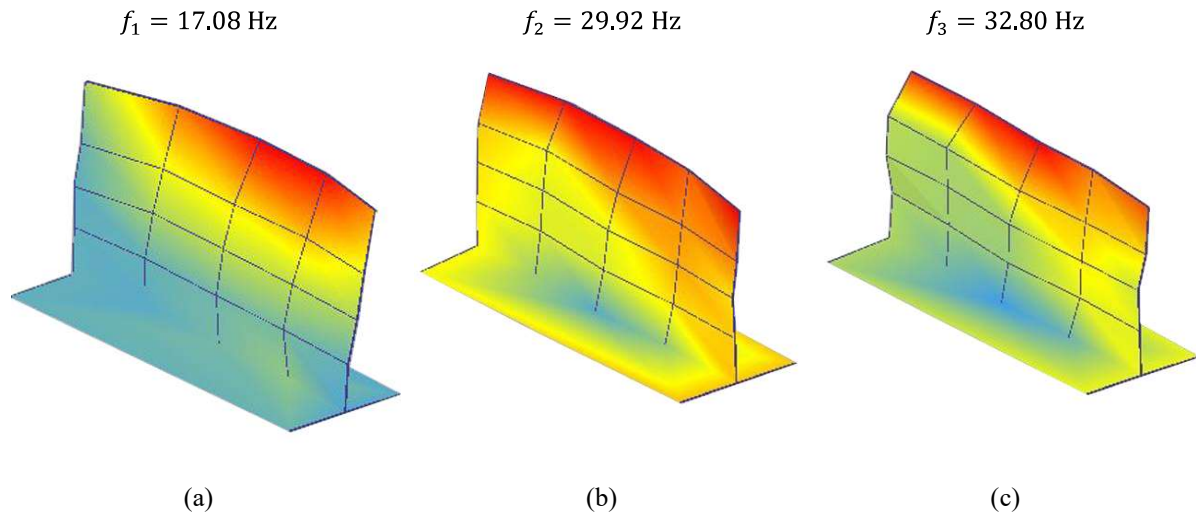
$$f_1 = 17.08 \text{ Hz} \qquad\qquad f_2 = 29.92 \text{ Hz} \qquad\qquad f_3 = 32.80 \text{ Hz}$$

(a)   (b)   (c)

Fig. 5. Natural vibration modes of the rammed earth model obtained from the DI-RE-IP-03 test: a) mode 1, b) mode 2, and c) mode 3

In order to verify the results obtained from modal analyses, the modal assurance criterion (MAC) was considered as an indicator of consistency or orthogonality between estimated modal vectors [46], as in Eq.1.

$$MAC_{k,l} = \frac{\left|\sum_{j=1}^{m} \Phi_j^k \Phi_j^l\right|^2}{\sum_{j=1}^{m}\left(\Phi_j^k\right)^2 \sum_{j=1}^{m}\left(\Phi_j^l\right)^2} \qquad\qquad\qquad \text{Eq. 1}$$

Where Φ_j^k and Φ_j^l are the eigenvectors associated to two eigenvalues k and I, while m is the number of degrees of freedom. The MAC was additionally considered to validate the damage estimation, as the evolution of damage can be quantified by the variation of the natural frequency of the modes. Yet, it must be guaranteed that the frequencies taken into account refer to the same mode shapes. Thus, the MAC of the modes being compared must be close to 1. Therefore, one considers the relation between natural frequency, mass and stiffness of a MDOF system (Eq. 2) [48]:

$$\left(2\pi f_{i,n}\right)^2 = \frac{K_{i,n}}{M_{i,n}} \qquad\qquad\qquad\qquad \text{Eq. 2}$$

and assuming isotropic damage [49] between the eigenvalue i in the first dynamic identification and in the dynamic identification n, as in Eq. 3 [50]:

$$K_{i,n} = \left(1 - d_{i,n}\right)K_{i,0} \qquad\qquad\qquad\qquad \text{Eq. 3}$$

Supposing that the seismic mass participating does not change significantly throughout the test, the damage indicator $d_{i,n}$ can be expressed as:

$$d_{i,n} = 1 - \left(\frac{f_{i,n}}{f_{i,0}}\right)^2 \qquad \text{Eq. 4}$$

In this formulation, the damage is a linear function of stiffness variation (e.g. pure tension) [51]. In the case of structures in which the dynamic behaviour depends on various modes and stiffness components (e.g. bending and shear stiffness), different relations between damage indicators and the variation of the frequencies might be assumed. Based on the shape of the first mode (out-of-plane bending) and assuming that the variation of the bending stiffness can be associated with a variation of the thickness of the wall (equivalent approach to consider the decrease of the bending stiffness due to the damage – cubic order variation) [52], the damage indicator is given by:

$$d_{i,n} = 1 - \left(\frac{f_{i,n}}{f_{i,0}}\right)^6 \qquad \text{Eq. 5}$$

Since changes in the natural frequencies of the model were detected in the last dynamic identification, the MAC was computed only between the vectors resulting from DI-RE-IP-01 and DI-RE-IP-03. The results showed a correspondence between the mode shape of the first frequency ($MAC = 0.76$), while no further correspondence was observed in other cases as $MAC < 0.1$, as expected (new local modes). Consequently, the damage indicator d (Eq. 5) was calculated only for frequency f_1, which resulted in d of 0.30. Although a damage indicator of 0.30 is far from 1.0 (theoretical full collapse and not expected to be achieved), it represents a relevant damage for this structure. However, since the self-weight of the wall closed the cracks after the loading tests, the effect of damage on the frequencies estimated from ambient vibration tests (low vibration amplitude) was reduced. In these cases, the proven occurrence of new local vibration modes may be considered an useful indicator of damage, more reliable than frequency decrease [53][54]. Finally, the accelerometers placed at the steel plate (base) allowed to conclude that the boundary conditions did not present significant alterations.

3.3 Displacement profiles

To better represent the displacements achieved during the cyclic tests, the vertical profiles of horizontal displacements considered the behaviour of both wing-walls individually in each direction (positive and negative). Hence, the envelope profiles are referred to the maximum and minimum values of horizontal displacements (d) recorded by the LVDTs (a1 to d1 and a5 to d5). Almost linear envelope profiles resulted up to the fourth cycle. Afterwards, the main horizontal crack in the web-wall opened, leading to a discontinuity in the displacement profiles (Fig. 6), which can be distinguished when the envelope of displacements of the right wing-wall

in the positive direction is considered. In fact, for the last two cycles, a large difference in the displacement of the LVDTs across the crack was detected (Fig. 6a), suggesting that the web-wall behaved as two overlapped blocks sliding along the formed crack.
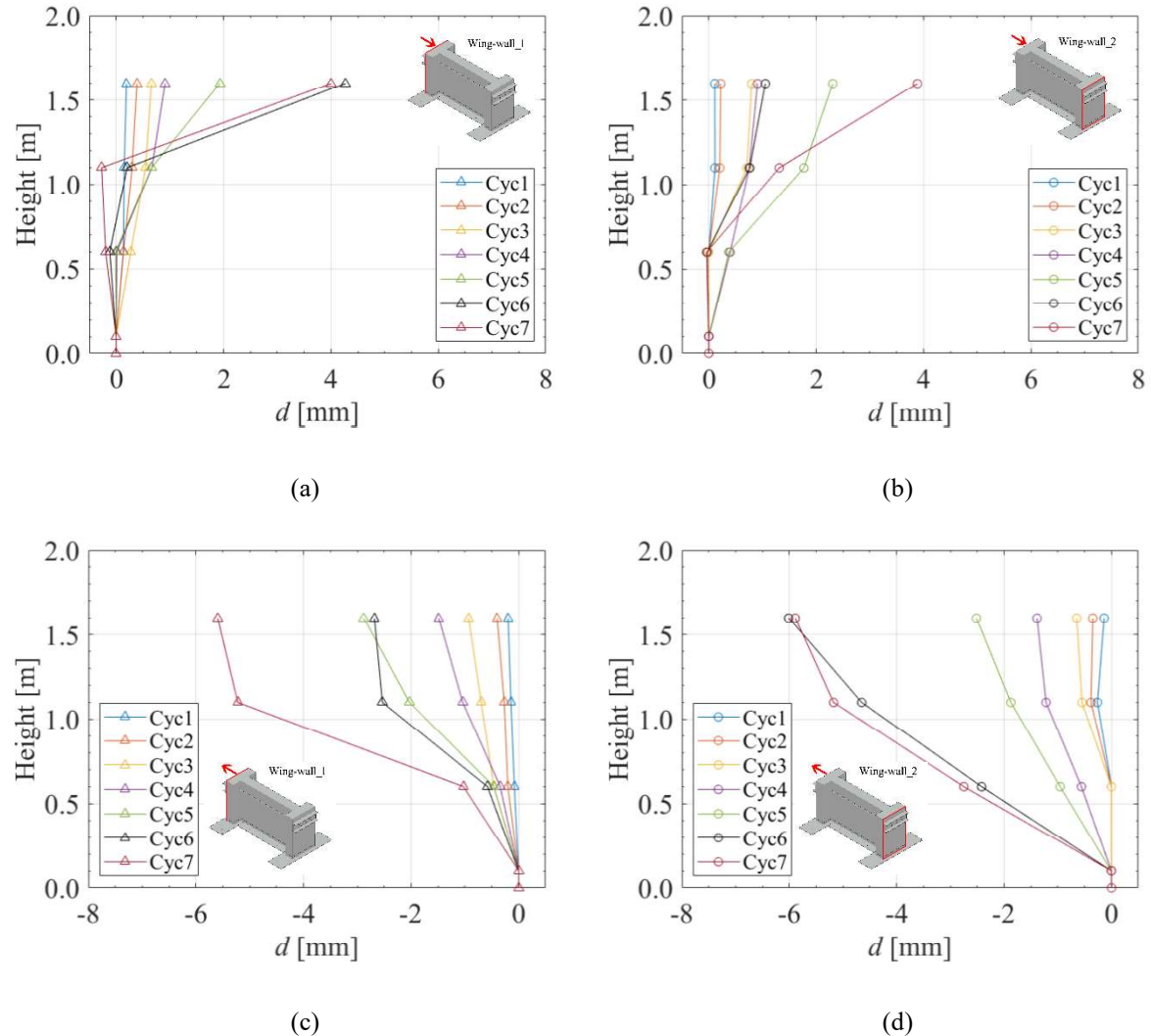

(a)

(b)

(c)

(d)

Fig. 6 *Envelope vertical profiles of horizontal displacements obtained for the model: a) left wing-wall in the positive direction, b) right wing-wall in the positive direction, c) left wing-wall in the negative direction, and c) right wing-wall in the negative direction*

3.4 Base shear coefficient

The results of the tests on the model are reported in Tab. 2 in terms of peak value of the applied force and corresponding horizontal displacement of the control point (CP). The results refer to each cycle and consider both positive (F_{peak}^+ and $d_{F_{peak}}^+$) and negative (F_{peak}^- and $d_{F_{peak}}^-$) loading directions, see also Fig. 2. Therefore, the corresponding base shear coefficient (BSC) was evaluated as the ratio of the base shear force (BSF) to the self-weight of the wall (W). The base shear force was assumed equal to the force measured by the actuator. Furthermore, the corresponding drift was calculated as the ratio of the displacement to the elevation of the

LVDT a1. The overall response curves of the cyclic tests are shown together with the envelope in Fig. 7a, while to distinguish the different response of the model due to the repetition of the loading path, the backbone of the response curves was analysed in both loading directions for each loop separately (see Fig. 7b and Fig. 7c). Fig. 7b illustrates that the BSC values of the two loops were similar along the linear branch. Afterwards, the BSC values decreased noticeably from the first to the second loop of a same cycle, particularly once the maximum capacity was achieved. Such difference between loops can be ascribed to the loss of cohesion in the rammed earth material, which eventually led to the opening of the main crack and marked nonlinear response, and the subsequent degradation of friction and interlocking mechanisms along the main crack. In addition, a comparison of the envelopes of both directions showed that the response of the model was similar up to the maximum BSC of the positive direction and differed hereafter (see Fig. 7c). In fact, while softening occurred for a displacement beyond the maximum BSC in the positive direction, the wall still exhibited increasing shear capacity for further negative displacements until attaining the maximum BSC in this direction, which was followed by a softening response. The different envelopes resulting from the two loading directions can be consequent to asymmetry generated by damage. Nevertheless, further contribution in such asymmetric response might be related to small misalignments of the test setup and variability in mechanical properties of the material.

The peak force in the positive direction was 93.18 kN and was achieved for a displacement of 0.900 mm during the fourth cycle, to which corresponds a BSC of 1.18 and a drift of 0.06%. While the peak force towards the negative direction was 109.14 kN and was reached with a displacement of 2.700 mm, which is equivalent to a BSC of 1.39 and a drift of 0.17%, respectively. Following the indications of NZS 4297 [39], the shear capacity of the RE-IP wall can be assumed equal to 80.64 kN. Therefore, the actual shear capacity of the RE-IP resulted 35% higher with respect to the nominal shear capacity calculated according to NZS 4297 [39].

Tab. 2 Main results of the cyclic test

Cycle	F^{+}_{peak} [kN]	BSC^{+}_{peak} [-]	$d^{+}_{F_{peak}}$ [mm]	Drift [%]	F^{-}_{peak} [kN]	BSC^{-}_{peak} [-]	$d^{-}_{F_{peak}}$ [mm]	Drift [%]
1	39.55	0.50	0.175	0.01	- 40.37	- 0.51	- 0.195	- 0.01
2	67.97	0.86	0.387	0.02	- 54.02	- 0.69	- 0.398	- 0.02
3	82.61	1.05	0.656	0.04	- 90.54	- 1.15	- 0.930	- 0.06
4	93.18	1.18	0.900	0.06	- 102.19	- 1.30	- 1.480	- 0.09

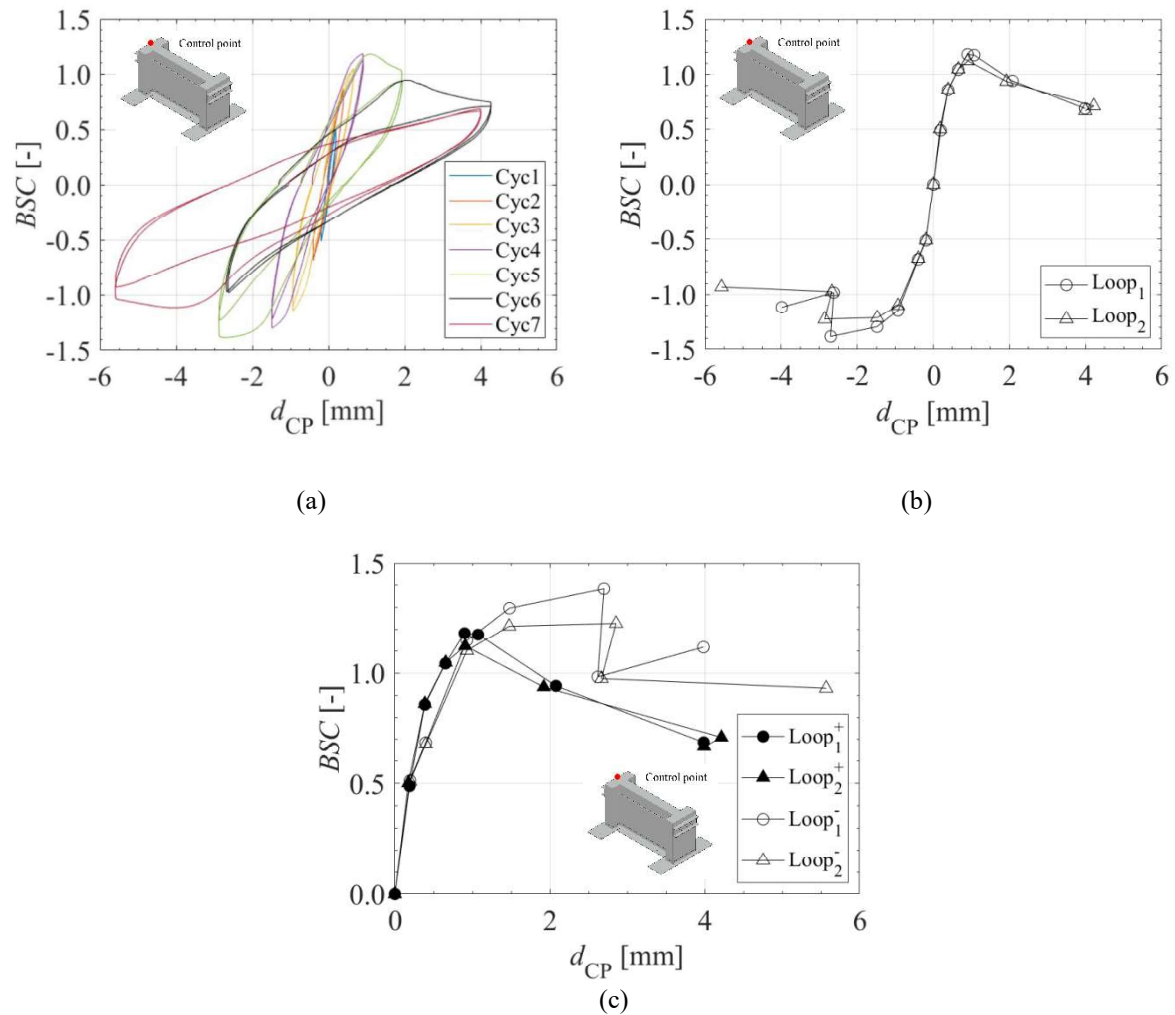| 5 | 92.66 | 1.18 | 1.075 | 0.07 | - 109.14 | - 1.39 | - 2.700 | - 0.17 |
| 6 | 74.25 | 0.94 | 2.080 | 0.13 | - 77.47 | - 0.98 | - 2.620 | - 0.16 |
| 7 | 54.12 | 0.69 | 3.987 | 0.25 | - 88.09 | - 1.12 | - 3.984 | - 0.25 |

(a)

(b)

(c)

Fig. 7 Response curve of the model: a) all cycles, b) overall envelope for each loading loop, and c) comparison between the negative and positive loading directions

The strength decay throughout the test was assessed to investigate the degradation of the structural sub-assembly due to increasing imposed cyclic displacement. For each cycle, two values of decay of the maximum absolute force were calculated for each loading direction, namely ΔF_1 and ΔF_2. According to the loading direction, each value of degradation refers to the maximum force of the first loop of a cycle ($F_{\text{Loop}_1}^{\text{cyc}}$), while considering the force values of the second loop of the same cycle ($F_{\text{Loop}_2}^{\text{cyc}}$) and of the first loop of the subsequent cycle ($F_{\text{Loop}_1}^{\text{cyc+1}}$) for the corresponding displacement value. Therefore, the decay values of the maximum force (ΔF_1 and ΔF_2) were calculated according to Eq. 6 and Eq. 7. Finally, according to the considered

loading direction, the force decay values were normalised through the overall peak force considering each direction separately while the displacement set for each step was normalised through the displacement at the overall peak force for each direction.

$$\Delta F_1 = F_{Loop_1}^{cyc} - F_{Loop_2}^{cyc} \qquad \text{Eq. 6}$$

$$\Delta F_2 = F_{Loop_1}^{cyc} - F_{Loop_1}^{cyc+1} \qquad \text{Eq. 7}$$

The resulting normalised decay of forces are illustrated in Fig. 8a and Fig. 8b, respectively, for ΔF_1 and ΔF_2. Although a defined relationship between the force decay and the displacement is not outlined, a trend can be observed for which the degradation ΔF_1 increased with the imposed displacement, as expected. Moreover, the force decay due to the second loop (ΔF_2) in the positive direction was higher than that of the first loop.
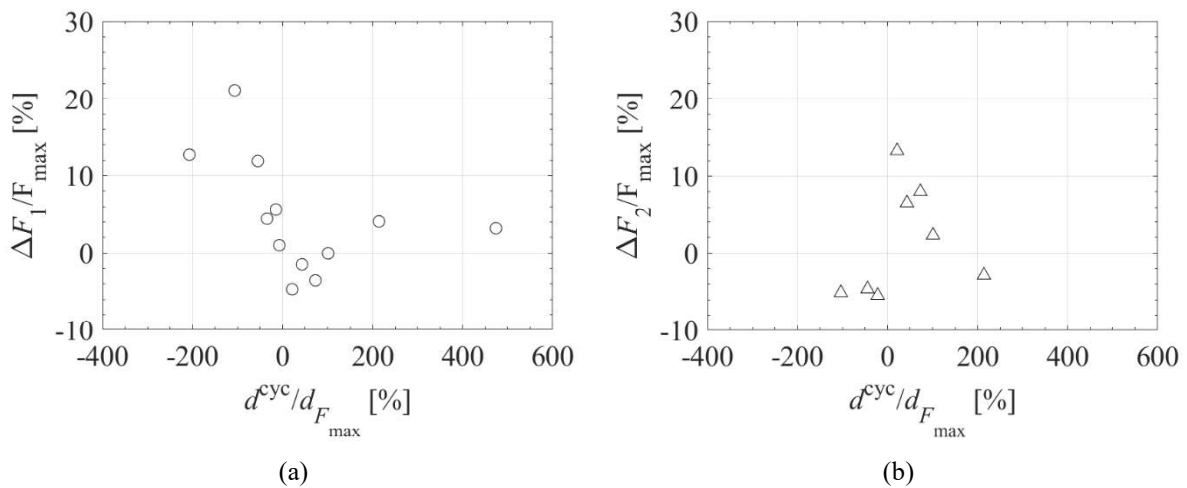

(a)   (b)

Fig. 8 *Force decay observed in the cyclic test of the model: a) first repetition, and b) second repetition*

3.5 Stiffness degradation

A further analysis of the degradation caused by the increasing cyclic displacement was conducted based on the evolution of the lateral stiffness. To this purpose, the lateral stiffness (K) decay throughout the cyclic test was computed with basis on the base shear force and the displacement of the control point. The stiffness was individuated for each loop and it was calculated according to different scenarios, namely positive loading $\left(K_{L_{Loop}^+}\right)$, positive unloading $\left(K_{UL_{Loop}^+}\right)$, negative loading $\left(K_{L_{Loop}^-}\right)$ and negative unloading $\left(K_{UL_{Loop}^-}\right)$. Meaning that, for each loop, the stiffness associated to the positive loading $\left(K_{L_{Loop}^+}\right)$ was evaluated in the range of 40% - 80% of the positive peak force by means of linear fitting; similarly, the stiffness associated to the negative loading $\left(K_{L_{Loop}^-}\right)$ considered the range 40% - 80% of the

negative peak force. In turn, the stiffness due to positive unloading $\left(K_{\mathrm{UL^+_{Loop}}}\right)$ was calculated considering 70% of the force associated to the positive peak displacement as the upper boundary till the complete unload of the structure; in such a way, only the unloading due to the reverse displacement of the cycle was taken into account. The same was performed for the stiffness due to negative unloading $\left(K_{\mathrm{UL^-_{Loop}}}\right)$, which was assessed in the range of 70% of the force associated to the negative peak displacement up to the complete unload of the structure. Afterwards, the values of stiffness were correlated with the cumulative displacement, which is the sum of the absolute values of displacement of the upper boundary of ranges up to that specific scenario, namely loading $\left(d_{\mathrm{cum}}^{K_{\mathrm{L}}}\right)$ and unloading $\left(d_{\mathrm{cum}}^{K_{\mathrm{UL}}}\right)$ as in Eq. 8 and in Eq. 9.

$$d_{\mathrm{cum}}^{K_{\mathrm{L}}} = \sum \left| d_{80\%F_{\mathrm{peak}}} \right| \qquad\qquad \text{Eq. 8}$$

$$d_{\mathrm{cum}}^{K_{\mathrm{UL}}} = \sum \left| d_{0\%post\_d_{\mathrm{peak}}} \right| \qquad\qquad \text{Eq. 9}$$

The loading and unloading stiffness degradation along the cyclic tests of the model are illustrated in Fig. 9a and Fig. 9b, respectively. It can be noted that both stiffnesses decrease with increasing cumulative displacement, as a consequence of the development of the cracks. In addition, for the same level of cumulative displacement, the stiffness associated to unloading was in general higher than that associated to loading. This can be explained by punching localised in the loading area that might occur at the beginning of the unload, while plastic displacement was still recorded by the LVDT at the control point; consequently, higher forces were required to involve the entire structure which in turn seemed stiffer.
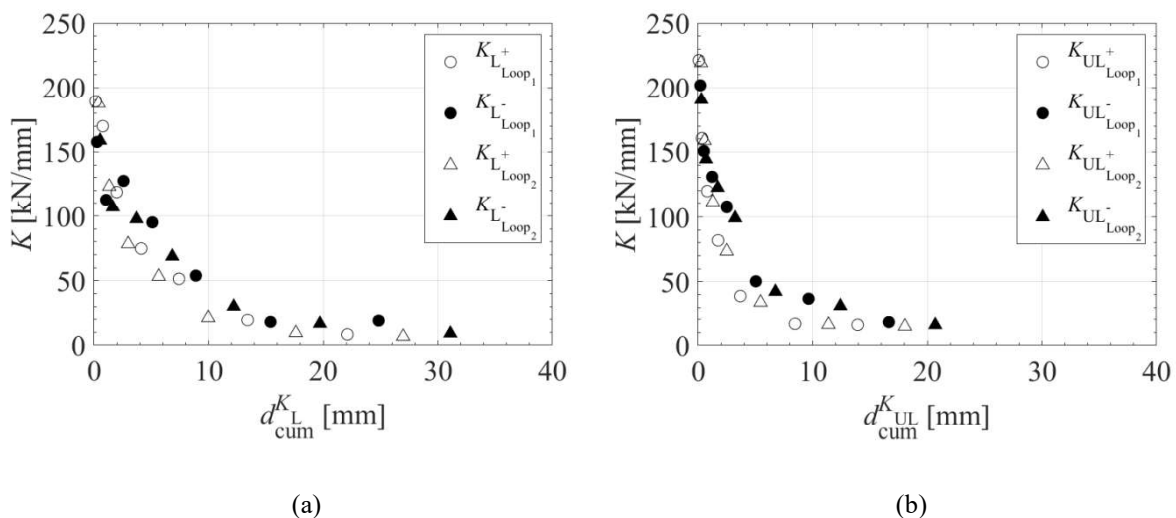

(a)   (b)

Fig. 9 *Stiffness degradation of the model: a) loading stiffness, and b) unloading stiffness*

3.6 Energy-based analysis

The energy dissipated by a building indicates its capacity to reduce the amplitude of displacements in response to a seismic event and consequently to reduce the ductility demand of a structure. Accordingly, to investigate the shear capacity of rammed earth walls, the energy dissipated by the structure was analysed as function of the input energy of the system for each loop and subsequently for each cycle. The dissipated energy for a complete loop $\left(E_{dis}^{Loop}\right)$ was evaluated as the integral of the force-displacement curve along the entire loop (Eq. 10); while the input energy $\left(E_{sys}^{Loop}\right)$ was calculated as the integral of the force-displacement curve along the single loading path, hence up to the positive peak displacement and the negative peak displacement (Eq. 11). From here, the dissipated energy $\left(E_{dis}^{cyc}\right)$ and the input energy $\left(E_{sys}^{cyc}\right)$ for each cycle is the sum of the corresponding components of the loops, as in Eq. 12 and in Eq. 13 respectively; while the cumulative dissipated energy $\left(E_{dis}^{cum}\right)$ is the cumulative sum of the dissipated energy along the test (Eq. 13) and the cumulative input energy $\left(E_{sys}^{cum}\right)$ is the cumulative sum of the input energy along the test (Eq. 14).

$$E_{dis}^{Loop} = \oint_{i=1:2}^{Loop} FdD \qquad \text{Eq. 10}$$

$$E_{sys}^{Loop} = \int_{0}^{D_{peak}^{+}} FdD + \int_{0}^{D_{peak}^{-}} FdD \qquad \text{Eq. 11}$$

$$E_{dis}^{cyc} = E_{dis}^{Loop_1} + E_{dis}^{Loop_2} \qquad \text{Eq. 12}$$

$$E_{sys}^{cyc} = E_{sys}^{Loop_1} + E_{sys}^{Loop_2} \qquad \text{Eq. 13}$$

$$E_{dis}^{cum} = \sum_{n}^{cycle} E_{dis}^{cyc} \qquad \text{Eq. 14}$$

$$E_{sys}^{cum} = \sum_{n}^{cycle} E_{sys}^{cyc} \qquad \text{Eq. 15}$$

The outcomes are illustrated in Fig. 10. A linear relationship was obtained between the input and the dissipated energy, in spite of considering loops, cycles or cumulative energy; while a ratio of dissipated energy to input energy was found to be in the range 44% - 61%. In

addition, the energies between two loops of a cycle were similar up to the fourth cycle $\left(E_{\text{dis}}^{\text{Loop}}\right)$; whereas, in the subsequent steps, the energies involved in the second loops decreased with respect to the first loops. This suggests that, once exceeding the elastic behaviour, the first loop of the cycle led to further plastic behaviour inducing damage to the structure, which was not recovered during the unloading, as further confirmed by the stiffness decay.
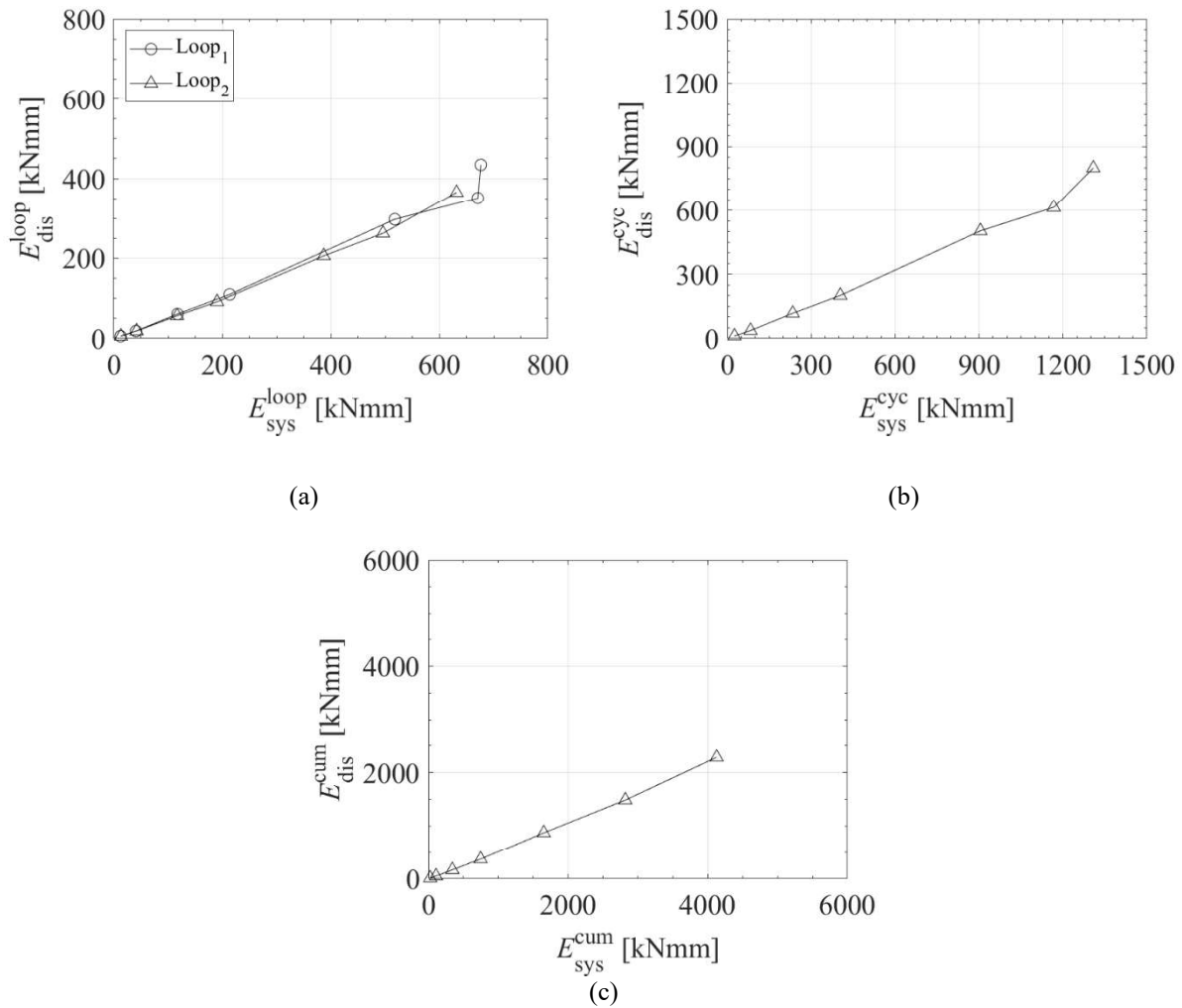

(a)

(b)

(c)

Fig. 10 *Dissipated and input energy of the model considering: a) loops, b) cycles, and c) cumulative energy*

Besides hysteretic dissipation, a system can dissipate energy by various non-conservative mechanisms (eg. friction, thermal effect, opening and closing of microcracks), which can occur at the same time and steadily decrease the free vibration of the structure itself. Such process is defined as elastic damping and identifying mathematically each of the mechanisms in an actual structure is inherently impossible. Therefore, the damping in a real building is idealised by an equivalent viscous damping coefficient (ξ_{eq}) in a manner that the associated dissipation of energy is equivalent to the energy dissipated in all the damping phenomena. In general, to accurately model the damping, the inelastic force-displacement relationship obtained from

experiments at slow rate of deformation is considered. In such a way, the energy dissipation due to rate-dependent effects is excluded. Such approach is based on the relationship between the dissipated energy and the stored strain energy per loading cycle as in (Eq. 16) [48].

$$\xi_{eq} = \frac{E_{dis}^{Loop}}{2\pi E_{sys}^{Loop}}$$

Eq. 16

Consistently with such approach, the equivalent damping coefficient (ξ_{eq}) was evaluated and is presented in Fig. 11 as a function of the corresponding input energy. It was observed that the equivalent damping coefficient (ξ_{eq}) is 7% for earlier cycles and increases to a peak of 10% at the last cycle; nonetheless an average value of 8% can be assumed for the overall inelastic response of the rammed earth structure. Such behaviour indicates that the equivalent damping increased with large displacements in the inelastic domain of the structure.
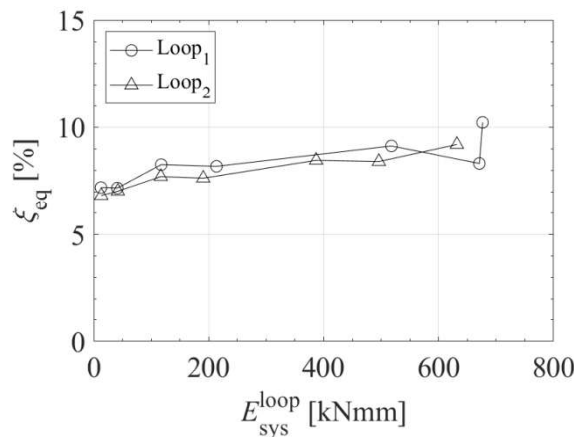
Fig. 11 *Equivalent damping coefficient of the model*

3.7 Bi-linear and linear equivalent systems

As the rammed earth wall demonstrated to dissipate hysteretic energy, an equivalent elastic-perfectly plastic system was idealized aiming at simplifying the non-linear behaviour; thus the bi-linear representation of the backbone curve was inferred following the indications given in [33][34][35][36]. Accordingly, the ultimate displacement (d_u) of the bi-linear curve was considered in correspondence to a decrease of 15% of F_{peak} of the experimental curve, while the secant stiffness (K) of the equivalent system was constrained to the 60% of F_{peak} of the original curve. Therefore, the yielding force (F_y) and displacement (d_y) of the simplified system were obtained by the equivalence of the energy of the experimental envelope curve and the energy of the idealised bi-linear curve. Afterwards, a further simplification was deduced through a linear representation, which intends to describe the experimental nonlinear response with an equivalent linear elastic structure. Therefore, the equivalent linear strength (F_e) was

evaluated by the equivalence of the energy between the linear curve and the bi-linear curve and assuming the same stiffness (K). Subsequently, the ductility factor (μ), the behaviour factor (q) and the reserve strength ratio, or overstrength, (γ) were estimated, as in Eq. 17, Eq. 18, Eq. 19 respectively. The ductility factor (μ) indicates the capacity of the actual structure to sustain large deformations beyond the yield point [33][34][35][36]. The behaviour factor (q) represents the ratio between the yielding force and the elastic force; therefore, in structural design, it can be an indicator of the dissipative capacity of the building (eg. $q = 1$ for non-dissipative structure, meaning that a brittle system should be designed for strength). The overstrength (γ) expresses the reserve of strength of the actual structure compared to the equivalent elastic-perfectly plastic system [33][34][35][36].

$$\mu = \frac{d_u}{d_y} \qquad\qquad\qquad \text{Eq. 17}$$

$$q = \frac{F_e}{F_y} \qquad\qquad\qquad \text{Eq. 18}$$

$$\gamma = \frac{F_{peak}}{F_y} \qquad\qquad\qquad \text{Eq. 19}$$

The parameters of the equivalent elastic-perfectly plastic and elastic systems are reported in Tab. 3 and in Fig. 12, while the simplification considered individually the envelope curves for negative and positive displacements. As a result, the comparison of the bi-linear curves obtained in the two directions leads to assume that the structure responded asymmetrically. In fact, the structural secant stiffness (K) for the positive direction was larger when compared to the one assessed for the negative direction. This might be a consequence of the cyclic test, which involved different levels of accumulated micro-cracks according to the two directions. On the other hand, the yielding force (F_y), displacement (d_y), and the elastic force were larger in the case of displacements towards the negative direction, which resulted from the higher experimental ultimate displacement (d_u) and higher peak force (F_{peak}). Nevertheless, the ductility factor, the behaviour factor and the overstrength were similar for both directions. In particular, the structure showed high ductility (μ) and behaviour factor (q), respectively, 4.17 and 2.71, indicating high dissipative capacity; whereas, the reserve of strength (γ) achieved 8% of the actual peak force.

Tab. 3 Parameters of the equivalent elastic-perfectly plastic and elastic systems for the rammed earth model RE-IP

Loading direction	F_y [kN]	d_y [mm]	K [kN/mm]	d_u [mm]	F_e [kN]	μ [-]	q [-]	γ [-]
Positive	85.97	0.457	188.23	1.809	226.21	3.96	2.63	1.08
Negative	102.83	0.888	115.84	3.698	278.45	4.17	2.71	1.06

(a)   (b)
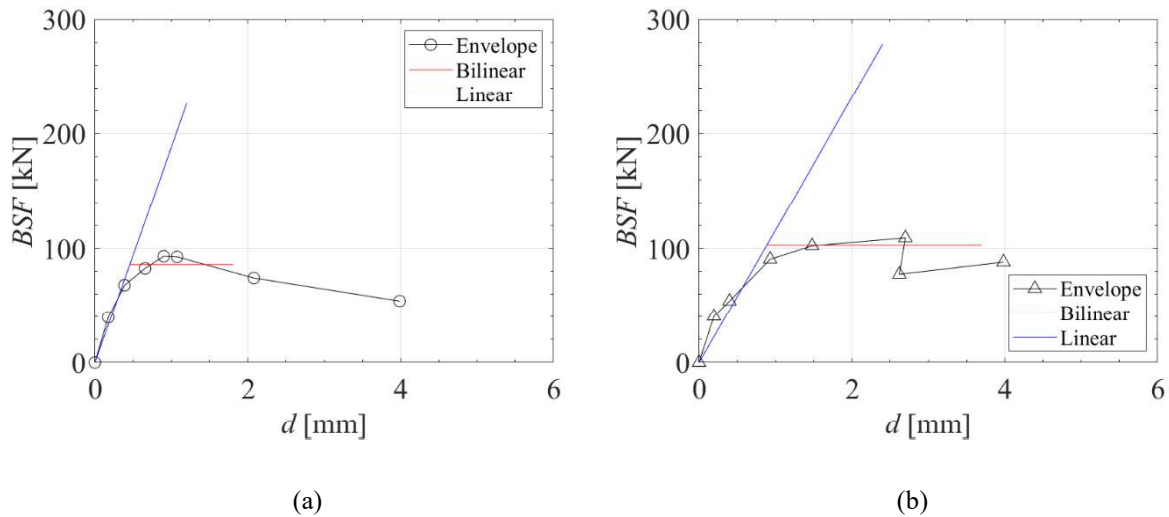
Fig. 12 Comparison of the non-linear experimental response with the equivalent elastic-perfectly plastic and elastic systems of the model: a) loading in the positive direction, and b) loading in the negative direction

4 Conclusions

This paper reports an experimental investigation of a rammed earth sub-assembly (RE-IP) consisting of an I-shaped wall model subjected to in-plane cyclic displacements. The crack pattern of the model demonstrated that a rammed earth wall subjected to low vertical loads and in-plane displacements cannot be assumed as a homogeneous material, as a horizontal fracture occurred along the interface between two layers. The performed dynamic identification tests aimed at quantifying the damage development through the in-plane cyclic tests, which attained a damage indicator of 0.30 and represents a significant damage for this model. With regard to the envelope of the *BSC*–displacement curves of the model, the response in the elastic branch was found to be similar between the loops. Afterwards, differences between the two envelopes were observed due to loss of cohesion of the material, and opening and development of the cracks.

As for the lateral stiffness, its degradation was found to be related to the increase in cumulative displacement. In addition, the analysis of the stiffness in the nonlinear branch indicated that the structure was in a plastic-deformation state that could be modified only by

exceeding the peak displacement of the previous step. Indeed, the stiffness associated to the second loop of a cycle resulted similar to the one related the first loop of the subsequent cycle. The dissipative capacity of the RE-IP model was also validated by an energy-based analysis. However, the energy values of the second loops decreased with respect to the first loops after the opening of the main crack. Thus, once the elastic behaviour was exceeded, the first loop of the cycle led to a further plastic domain, which was not recovered during the unloading path. From here, the equivalent damping coefficient was observed to slightly increase with large displacement demands, confirming the non-conservative processes that occurred in the inelastic domain. Therefore, based on the dissipative capacity of the model, equivalent elastic and elastic-perfectly plastic systems were inferred considering the two loading directions separately. As a result, different yielding force and displacement values were obtained; nevertheless, the lateral stiffness, ultimate displacement, ductility factor, behaviour factor and overstrength values were similar in both directions.

5 Statement and Declarations

The authors have no conflicts of interest to declare that are relevant to the content of this article.

6 Acknowledgments

7 Author contributions

Romanazzi A. – Conceptualization, methodology, acquisition of data, data analysis, formal analysis, investigation, writing – original draft, review and editing, visualization.

Oliveira D.V. – Conceptualization, methodology, writing – review and editing, supervision, funding acquisition

8 References

[1] Jaquin, P. A., Augarde, C. E., and Gerrard, C. M. (2008) Chronological description of the spatial development of rammed Earth techniques. International Journal of Architectural Heritage, 2, 377 - 400. https://doi.org/10.1080/15583050801958826

[2] Pacheco-Torgal, F., and Jalali, S. (2012) Earth construction: Lessons from the past for future eco-efficient construction. Construction and Building Materials, 29, 512 - 519. https://doi.org/10.1016/j.conbuildmat.2011.10.054

[3] Ciancio, D., Jaquin, P., and Walker, P. (2013) Advances on the assessment of soil suitability for rammed earth. Construction and Building Materials, 42, 40 - 47. https://doi.org/10.1016/j.conbuildmat.2012.12.049

[4] Morel, J.C., Mesbah, A., Oggero, M., and Walker, P. (2001) Building houses with local materials: means to drastically reduce the environmental impact of construction. Building and Environment, 36, 1119 - 1126. https://doi.org/10.1016/S0360-1323(00)00054-8

[5] Correia, M., Varum, H., and Lourenço, P.B. (2015) Common damages and recommendations for the seismic retrofitting of vernacular dwellings. In M. R. Correia, P. B. Lourenço, and H. Varum (Eds.), Seismic Retrofitting: Learning from Vernacular Architecture. Taylor & Francis Group, London.

[6] Lacoutre, L.E.Y., Bernal, P.C., Ortiz, J. C.R., and Valencia, D.R. (2007) Estudios de vulnerabilidad sísmica, rehabilitación y refuerzo de casas en adobe y tapia pisada. Apuntes: Revista de Estudios Sobre Patrimonio Cultural, 20, 286 - 303.

[7] Lourenço, P. B., Torrealva, D., Cancino, C., Wong, K., Karanikoloudis, G., and Ciocci, M. P. (2017) Innovative traditional technologies for rehabilitation and protection of earthen structures: the Getty conservation institute seismic retrofitting project. Proceeding of the 3rd International Conference on Protection of Historical Constructions, Lisbon, 12th - 15th July, 12 - 15.

This paper can be found at https://link.springer.com/article/10.1617/s11527-022-01894-z

[8] Bui, T.T., Bui, Q.B., Limam, A., and Maximilien, S. (2014) Failure of rammed earth walls: From observations to quantifications. Construction and Building Materials, 51, 295 - 302. https://doi.org/10.1016/j.conbuildmat.2013.10.053

[9] Liu, K., Wang, M., Wang, Y. (2015) Seismic retrofitting of rural rammed earth buildings using eternally bonded fibers. Construction and Building Materials, 100, 91 - 101. https://doi.org/10.1016/j.conbuildmat.2015.09.048

[10] Romanazzi, A., Oliveira, D.V., and Silva, R.A. (2019) Experimental investigation on the bond behavior of a compatible TRM-based solution for rammed earth heritage. International journal of architectural heritage. https://doi.org/10.1080/15583058.2019.1619881

[11] Romanazzi, A., Van Gorp, M., Oliveira, D.V., Silva, R.A., and Verstrynge, E. (2019) Experimental shear behaviour of rammed earth strengthened with a TRM-based compatible technique. Key Engineering Materials, 817, 544 – 551. https://doi.org/10.4028/www.scientific.net/KEM.817.544

[12] El-Nabouch, R., Bui, Q. B., Plé, O., and Perrotin, P. (2017) Assessing the in-plane seismic performance of rammed earth walls by using horizontal loading tests. Engineering Structures, 145, 153 - 161. https://doi.org/10.1016/j.engstruct.2017.05.027

[13] Maniatidis, V., and Walker, P. (2008) Structural capacity of rammed earth in compression. Journal of Materials in Civil Engineering, 20, 230 - 238. https://doi.org/10.1061/(ASCE)0899-1561(2008)20:3(230)

[14] Miccoli, L., Oliveira, D.V., Silva, R. ., Müller, U., and Schueremans, L. (2015) Static behaviour of rammed earth: experimental testing and finite element modelling. Materials and Structures, 48, 3443 - 3456. https://doi.org/10.1617/s11527-014-0411-7

[15] Silva, R. A., Oliveira, D. V., Miccoli, L., and Schueremans, L. (2014) Modelling of rammed earth under shear loading. Proceeding of the 9th International Conference on Structural Analysis of Historical Constructions, Mexico City, 14th - 17th October.

[16] Bui, Q. B., Bui, T. T., Tran, M. P., Bui, T. L., and Le, H. A. (2019) Assessing the seismic behavior of rammed earth walls with an L-Form cross-section. Sustainability, 11, 1296. https://doi.org/10.3390/su11051296

[17]   Bui, Q. B., Limam, A., and Bui, T. T. (2018) Dynamic discrete element modelling for seismic assessment of rammed earth walls. Engineering Structures, 175, 690 - 699. https://doi.org/10.1016/j.engstruct.2018.08.084

[18]   Bui, Q. B., and Bui, T. T. (2020) Seismic behaviour of rammed earth walls: a time history analysis. In: Ha-Minh C., Dao D., Benboudjema F., Derrible S., Huynh D., Tang A. (eds) CIGOS 2019, Innovation for Sustainable Infrastructure. Lecture Notes in Civil Engineering, vol 54.

[19]   Bui, T. T., Bui, Q. B., Limam, A., and Morel, J.-C. (2016) Modeling rammed earth wall using discrete element method. Continuum Mechanics and Thermodynamics, 28, 523 - 538. https://doi.org/10.1007/s00161-015-0460-3

[20]   Barros, R.S., Costa, A., Varum, H., Rodrigues, H., Lourenço, P.B., and Vasconcelos, G. (2015) Seismic behaviour analysis and retrofitting of a row building. In Seismic Retrofitting: Learning from Vernacular Architecture.

[21]   Allahvirdizadeh, R., Oliveira, D.V., and Silva, R.A. (2019) Numerical modeling of the seismic out-of-plane response of a plain and TRM-strengthened rammed earth subassembly. Engineering Structures, 193, 43 - 56. https://doi.org/10.1016/j.engstruct.2019.05.022

[22]   Allahvirdizadeh, R., Oliveira, D.V., and Silva, R.A. (2021) Numerical investigation of the in-plane seismic performance of unstrengthened and TRM-strengthened rammed earth walls. International Journal of Architectural Heritage, 15, 548 - 566. https://doi.org/10.1080/15583058.2019.1629507

[23]   Miccoli, L., Drougkas, A., and Müller, U. (2016) In-plane behaviour of rammed earth under cyclic loading: Experimental testing and finite element modelling. Engineering Structures, 125, 144 - 152. https://doi.org/10.1016/j.engstruct.2016.07.010

[24]   Tomaževič, M., and Lutman, M. (1996) Seismic behavior of masonry walls: modeling of hysteretic rules. Journal of Structural Engineering, 122, 1048 - 1054. https://doi.org/10.1061/(ASCE)0733-9445(1996)122:9(1048)

[25]   Reyes, J.C., Smith-Pardo, J.P., Yamin, L.E., Galvis, F. A., Sandoval, J.D., Gonzalez, C.D., and Correal, J.F. (2019) In-plane seismic behavior of full-scale earthen walls with openings retrofitted with timber elements and vertical tensors. Bulletin of Earthquake Engineering, 17, 4193 - 4215. https://doi.org/10.1007/s10518-019-00601-8

This paper can be found at https://link.springer.com/article/10.1617/s11527-022-01894-z

[26] Reyes, J. C., Yamin, L. E., Hassan, W. M., Sandoval, J. D., Gonzalez, C. D., and Galvis, F. A. (2018) Shear behavior of adobe and rammed earth walls of heritage structures. Engineering Structures, 174, 526 - 537. https://doi.org/10.1016/j.engstruct.2018.07.061

[27] Zhou, T., Liu, B., Zhao, X., and Mu, J. (2018) Experimental testing of the in-plane behavior of bearing modern rammed earth walls. Advances in Structural Engineering, 21, 2045 - 2055. https://doi.org/10.1177/1369433218764978

[28] El-Nabouch, R., Bui, Q.B., Plé, O., Perrotin, P., Poinard, C., Goldin, T., and Plassiard, J.P. (2016) Seismic assessment of rammed earth walls using pushover tests. Procedia Engineering, 145, 1185 - 1192. https://doi.org/10.1016/j.proeng.2016.04.153

[29] Arslan, M.E., Emiroğlu, M., Yalama, A. (2017) Structural behavior of rammed earth walls under lateral cyclic loading: a comparative experimental study. Construction and Building Material,133, 433 - 42. https://doi.org/10.1016/j.conbuildmat.2016.12.093

[30] Wang, Y., Wang, M., Liu, K., Pan, W., Yang, X. (2017) Shaking table tests on seismic retrofitting of rammed-earth structures. Bulletin of Earthquake Engineering, 15, 1037 - 1055. https://doi.org/10.1007/s10518-016-9996-2

[31] Silva, R.A., Mendes, N., Oliveira, D.V., Romanazzi, A., Domínguez-Martínez, O., and Miranda, T. (2018) Evaluating the seismic behaviour of rammed earth buildings from Portugal: From simple tools to advanced approaches. Engineering Structures, 15, 144 - 156. https://doi.org/10.1016/j.engstruct.2017.12.021

[32] Bui, Q.-B., Hansa, S., Morel, J.-C., Do, A.-P. (2011) First exploratory study on dynamic characteristics of rammed earth buildings. Engineering Structures, 33, 3690 - 3695. https://doi.org/10.1016/j.engstruct.2011.08.004

[33] BS EN 1998-1. (2004) Eurocode 8: Design of structures for earthquake resistance - Part 1: General rules, seismic actions and rules for buildings. European Committee for Standardization.

[34] Consiglio Superirore dei Lavori Pubblici. (2008) Nuove norme techniche per le costruzioni, D.M. Infrastrutture 14/01/2008.

[35] Tomaževič, M. (1997) Seismic design of masonry structures. Progress in Structural Engineering and Materials, 1, 88 - 95.

[36] Tomaževič, M. (2006) Earthquake resistant design of masonry buildings. In Series on Innovation in Structures and Construction - Vol. 1 (Vol. 1). Imperial College Press.

[37] Carvalho, E.C. (1998) Seismic testing of structures. Proceeding of the 11th European Conference on Earthquake Engineering, Paris, 6th - 11th September..

[38] Houben, H., and Guillaud, H. (1994) Earth construction: A comprehensive guide. Intermediate Technology Publications.

[39] NZS 4297. (1998). Engineering design of earth buildings. *Wellington: Standards New Zealand.*

[40] Ghalishooyan, M., and Shooshtari, A. (2015) Operational modal analysis techniques and their theoretical and practical aspects: a comprehensive review and introduction. Proceeding of the 6th International Operational Modal Analysis Conference, Gijón, 12th - 14th May.

[41] Zhang, L., Brincker, R., and Andersen, P. (2004) An overview of major developments and issues in modal identification. Proceedings of the 22nd IMAC Conference and Exposition on Structural Dynamics, Dearborn, 26th - 29th January.

[42] ARTeMIS. (2013) Ambient response testing and modal identification software. SVS – Structural Vibration Solutions A/S. Modal 2.5. Denmark.

[43] Pepi, C., Cavalagli, N., Gasuella, V., and Gioffrè, M. (2021) Damage detection via modal analysis of masonry structures using shaking table tests. Earthquake Engineering and Structural Dynamics, 50, 2077 - 2097. https://doi.org/10.1002/eqe.3431

[44] Ren, W.X., and De Roeck, G. (2002) Structural damage identification using modal data. I: simulation verification. Journal of Structural Engineering, 128, 87 - 95. https://doi.org/10.1061/(ASCE)0733-9445(2002)128:1(87)

[45] Brownjohn, J.M.W., De Stefano, A., Xu, Y.L., Helmut, W., and Aktan, A. (2011) Vibration-based monitoring of civil infrastructure: challenges and successes. Journal of Civil Structural Health Monitoring, 1, 79 - 95. https://doi.org/10.1007/s13349-011-0009-5

[46] Ewins D.J. (2000). Modal testing: theory, practice and application. 2nd Edition, Research Studies Press LTD, Baldock, Hertfordshire, England.

[47] Swagato, D., Purna, S., and Sanjaya, P. (2016) Vibration-based damage detection techniques used for health monitoring of structures: a review. Journal of Civil Structural Health Monitoring, 6, 477 - 507. https://doi.org/10.1007/s13349-016-0168-5

[48] Chopra, A.K. (2012) Dynamics of structures: theory and applications to earthquake engineering (W. J. Hall, Ed.). Prentice Hall.

[49] Lemaitre, J., and Desmorat, R. (2005) Engineering damage mechanics: ductile, creep, fatigue and brittle failures. Springer Berlin Heidelberg.

[50] Candeias, P. (2008) Avaliação da vulnerabilidade sísmica de edifícios de alvenaria. (Seismic vulnerability assessment of ancient buildings). PhD Thesis, Universidade do Minho.

[51] Mendes, N. (2012) Seismic assessment of ancient masonry buildings: shaking table tests and numerical analysis. PhD Thesis, Universidade do Minho.

[52] Giordano, E., Mendes, N., Masciotta, M., Clementi, F., Sadeghi, N., Silva, R.A., and Oliveira D.V. (2020) Expeditious damage index for arched structures based on dynamic identification testing. Construction and Building Materials, 265, 120236. https://doi.org/10.1016/j.conbuildmat.2020.120236

[53] Koushik, R. (2017) Structural damage identification using mode shape slope and curvature. Journal of Engineering Mechanics, 143, 04017110. https://doi.org/10.1061/(ASCE)EM.1943-7889.0001305

[54] Yazdanpanah, O., Seyedpoor, S.M., and Akbarzadeh Bengar, H. (2015) A new damage detection indicator for beams based on mode shape data. Structural Engineering and Mechanics, 53, 725 - 744. https://doi.org/10.12989/sem.2015.53.4.725